

Dissipative self-organization in optical space

Chad Ropp^{1,4}, Nicolas Bachelard^{1,4}, David Barth¹, Yuan Wang^{1,2} and Xiang Zhang^{1,2,3*}

The complex behaviours of schools of fish¹ and swarms of bacteria^{2,3} can be emulated in soft-matter systems that assemble into flocks^{4,5} and active nematics⁶, respectively. These artificial structures emerge far from thermodynamic equilibrium through the process of dissipative self-organization, in which many-body interactions coordinate energy dissipation. The development of such active matter has deepened our understanding of living systems. Yet, the application of dissipative self-organization has been restricted to soft-matter systems, whose elements organize through their respective motions. Here, we demonstrate dissipative self-organization in solid-state photonics. Our structure consists of a random array of Fabry–Pérot resonators that are externally driven and interact coherently through thermo-optical feedback. At sufficient optical driving power, the system undergoes a phase transition into a robustly organized non-equilibrium state that actively partitions energy dissipation, while displaying resiliency to perturbations and collective memory^{7,8}. Self-organizing photonics opens possibilities for developing scalable architectures and life-like networks for brain-inspired computation^{9,10}.

In dissipative self-organization, the coordination of energy dissipation through many-body interactions leads to the emergence of order far from thermodynamic equilibrium¹¹. This process is prevalent in nature and observable in systems ranging from flocking birds¹² to weather patterns¹³. Artificial realizations of dissipative self-organization have been achieved in soft-matter systems that are externally driven, typically through mechanical^{14,15}, chemical^{15,16}, electric^{3,17} or magnetic means^{18,19}. By continuously balancing energy dissipation with supply, many-body interactions maintain the system in a stable configuration that can exhibit life-like adaptability¹¹, a memory of dissipation history^{7,8}, and often remarkable functionalities. As examples, hydrodynamic interactions can produce symmetry-broken flocking⁵ and asymmetric phonon propagation^{14,20}, while coherent wave interactions have led to the self-organization of self-healing bandgap crystals²¹. So far, the application of dissipative self-organization has been limited to soft-matter systems, in which the coordination of dissipation is achieved through the motion of elements. Developing this concept in solid-state photonics could enable the formation of new devices that are dynamically reconfigurable and embedded with life-like functionalities. Such collective architectures might help realize new states of driven matter^{22,23} and all-optical platforms for collective memory and neuromorphic computation^{9,10}.

Here, we report a solid-state system that is driven far from equilibrium and organizes with self-adaptive order through dissipative self-organization. Our silicon-based structure consists of a disordered array of Fabry–Pérot resonators (Fig. 1a) that are driven by a continuous-wave laser. Under coherent driving, dissipative self-organization is revealed as a phase ordering between elements²¹. For optical waves, phase is accumulated in space by the product of xn —which we define

as the optical space—where x is the real-space distance and n is the refractive index²⁴. Here, the role of motion, Δx , can be substituted by changes in the refractive index, Δn . This equivalency enables dissipative self-organization to be applied to solid-state platforms that organize through changes in the refractive indices of elements.

When the one-dimensional array of thermally insulated resonators is exposed to a coherent drive, the absorption of the drive by the elements leads to local increases in temperature (see Methods). Phase organization arises spontaneously due to thermo-optical²⁵ feedback between wave scattering and absorptive heating. Even though the elements are fixed in space, their increase in temperature leads to a growth in optical length, defined as $ln_i(T_i)$, where l is the physical length, T_i is the temperature and $n_i(T_i)$ is the temperature-dependent refractive index of the i th resonator. Eventually, a steady-state configuration characterized by an ordered optical-phase distribution is reached (Fig. 1b). Similar dynamic ordering emerges regardless of the random spacing between elements (Supplementary Fig. 1). A typical time evolution is shown in Fig. 1c, which illustrates the dynamics of the phase ordering when driven at 1,064 nm. The corresponding non-uniform temperature dynamics (Fig. 1d) emphasize that this system self-organizes far from equilibrium by collectively balancing the input energy with thermal dissipation, defined as $j_{\text{th},i}(t) = 4hT_i(t)$ for the i th resonator (see Methods). During the transient evolution the total dissipation, $j_{\text{th}}(t) = \sum_N j_{\text{th},i}(t)$, monotonically increases toward a maximum at steady state (red curve in Fig. 1d). While the synchronization^{26,27} and the locking²⁸ of amplified modes have been reported in nonlinear photonic platforms, here collective phase ordering arises entirely through dissipation amongst passive elements.

The emergent phase order is revealed by the formation of a depletion band in the transmission spectrum, whose edge is fixed to the wavelength of the drive (observed numerically in Fig. 1e). This response is experimentally confirmed using an array of thermally insulated silicon resonators (see Methods and Supplementary Fig. 2). Our sample is driven by a laser diode (1,064 nm) and the transmission spectrum is probed using a counter-propagating supercontinuum laser (Fig. 2a; see Methods). At low drive power (that is, before self-organization) the transmission spectrum is featureless around 1,064 nm (black curve in Fig. 2b). At higher power a depletion band emerges with an edge fixed by the wavelength of the drive (dark red and red curves in Fig. 2b). This feature is reproducible and experimentally observed in many samples with different slab thicknesses and random spacings, as well as in samples with up to 12 elements (Supplementary Fig. 3). Numerical simulations also show that the depletion band can be spectrally tuned by dynamically changing the drive wavelength (Supplementary Fig. 4). Similar gapped responses can emerge in coherently driven ensembles of mobile scatterers that uniformly dissipate kinetic energy²¹. Here, this feature arises through the non-uniform dissipation of thermal energy, which suggests that a more general phenomenon may

¹NSF Nanoscale Science and Engineering Center, University of California, Berkeley, CA, USA. ²Materials Sciences Division, Lawrence Berkeley National Laboratory, Berkeley, CA, USA. ³University of Hong Kong, Hong Kong, China. ⁴These authors contributed equally: Chad Ropp, Nicolas Bachelard.

*e-mail: xiang@berkeley.edu

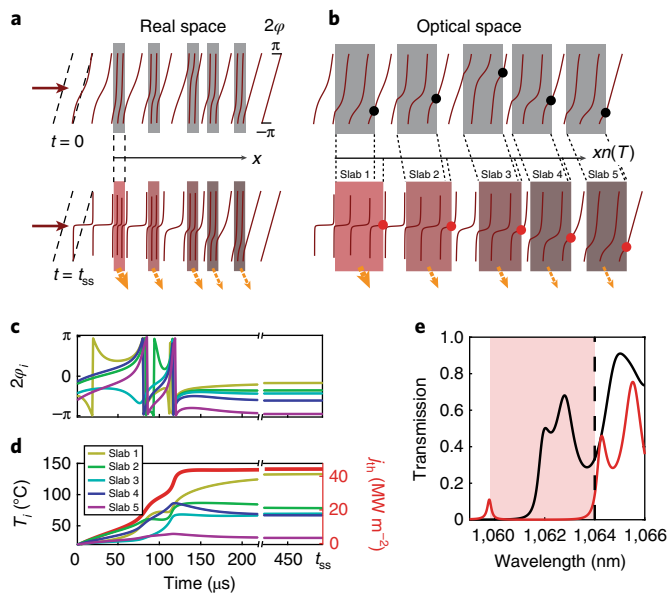


Fig. 1 | Self-organization of optical phase. **a**, Diagram depicting the structure in real space. A coherent drive (red arrow) propagates through a random array of thermally insulated Fabry–Pérot resonators (grey slabs). The phase distribution for the drive field’s intensity, 2φ (red lines), is plotted along with the forward-propagating component of the phase (dashed lines). Thermo-optical feedback between wave scattering and heat dissipation (orange arrows) drives the elements, initially at room temperature ($t=0$), towards a non-equilibrium steady state ($t=t_{ss}$) with a non-uniform thermal distribution (red-to-grey colour). **b**, In optical space—where physical distances x are replaced by optical distances xn —the elements’ effective sizes increase with temperature (growth shown with dashed lines). The phase evolves from an initially disordered (black dots) to an ordered (red dots) distribution. **c**, Simulated dynamics of the phase distribution during the self-organization of five randomly placed 10.5- μm -thick silicon slabs. **d**, Simulated dynamics of individual temperatures. On average, the elements closer to the drive reach higher temperatures; however, monotonic temperature ordering is not required. The total dissipation j_{in} increases towards a maximum at steady state (red curve). **e**, Transmission spectrum before ($t=0$, black) and after ($t=t_{ss}$, red) self-organization, with the emergent depletion band highlighted in red.

govern the emergence of phase order in systems that dissipate coherent energy.

The system undergoes a phase transition into a locked configuration—self-sustained despite increasing drive power—which demonstrates signatures of dissipative adaptation⁷. Below 80 mW, increasing the drive power causes spectral features to redshift (Fig. 2c), while both the distribution of temperatures and the total dissipation evolve erratically (Fig. 2d). Above this threshold power, the depletion band emerges and the spectrum remains unchanged despite increases in the drive power (dark red and red curves in Fig. 2b and intensity plot in Fig. 2c). This spontaneous ordering of the photonic response describes a phase transition into a highly dissipative ‘locked steady state’ characterized by a sudden increase in j_{in} (red curve in Fig. 2d). This state displays signatures of an adaptive partitioning of energy dissipation, as illustrated by individual temperatures, which evolve linearly with drive power above the threshold (fitted dashed lines in Fig. 2d). The spontaneous coordination of energy dissipation is a hallmark of dissipative self-organization²⁹, with phase transitions into organized states also observed in different systems^{5,30}. Here, optical absorption produces a strong intensity-dependent response, which is in contrast

to the intensity-independent order emerging in systems that uniformly distribute and dissipate kinetic energy through the transfer of momentum²¹. The experimental temperatures plotted in Fig. 2d are extracted from the radiation of the slabs, which are obtained through thermal imaging (Fig. 2e) and calibrated using the spectral response of isolated slabs (see Methods and Supplementary Fig. 5). All measurements are taken at steady state, which is reached after a transient time of $\sim 250 \mu\text{s}$ (Supplementary Fig. 6b).

The properties of self-adaptation are enforced by a strong attraction towards the locked steady state, which produces a dynamic response robust to external perturbations. The resiliency of our sample to thermal perturbations is probed by modulating its temperature with a blue laser that is incident from out of plane (see Methods). With the drive off, the structure responds strongly to the blue-laser perturbation as seen by the large variation in the transmission spectrum (Fig. 3a). Above the phase transition, this variation is reduced and the transmission spectrum appears robustly locked (Fig. 3b). The transition from the unlocked to the locked regime is revealed in Fig. 3c, which plots the spectral decorrelation in response to the perturbation as a function of the drive power (see Methods). Just before the transition we see a dramatic increase in decorrelation due to a bifurcation effect. At this transition, the perturbation forces the system to jump back and forth between the locked and unlocked states, resulting in large changes in the transmission spectrum. At lower power the system is sustained in an unlocked steady state with higher decorrelation than the locked state, which probably has a stronger basin of attraction. In this locked state, robustness originates from a spontaneous reconfiguration of the thermal distribution (Supplementary Fig. 7a–c), which tends to reduce the average rise in temperature of the ensemble. This robustness is reinforced by increasing the number of elements in the system (Supplementary Fig. 7d). Similar adaptive behaviours have been observed in other non-equilibrium systems^{21,31–33}, where collective resiliency to perturbation arises through the continuous and nonlinear attraction towards steady state.

The existence of bifurcations in our system leads to collective memory effects that are revealed through adiabatic tuning of the drive intensity. We observe hysteresis in the temperature profile of a four-slab sample when scanning across the phase transition (Fig. 4a and Supplementary Fig. 8). The direction of hysteresis indicates that the structure tends to remain in a higher dissipative state even when the drive is reduced below the original transition power. Hysteresis is observable in single slabs and originates from the interaction between the drive and the Fabry–Pérot resonance (Supplementary Fig. 9a–c). With increasing drive power a bifurcation leads to the coexistence of two dynamic attractors (Supplementary Fig. 9d,e). The thermal configuration before bifurcation determines toward which steady-state attractor the system converges. While hysteresis has been reported previously in self-organized structures^{34–36}, here, collective memory is observed, leading to the emergence of hidden states only accessible through specific driving schemes. These states are not observable with single slabs, but instead require a higher dimensionality, provided by multiple slabs. An example of such a state appears within the phase transition of a five-slab structure with decreasing power (Fig. 4b,c). This state (labelled in Fig. 4c) differs from other observed states in both its transmission spectrum and thermal profile. The thermal profile of the hidden state shows more elevated temperatures (corresponding to higher dissipation) than its degenerate state, as well as a unique temperature distribution in which the second slab is the hottest (insets in Fig. 4b,c). Path-dependent responses make any analytical interpretations of the steady-state condition challenging; however, we observe a tendency for the system to remain in higher dissipative states as it traverses circuitous trajectories in phase space (see Supplementary Fig. 10 for a simulated example). Such trajectories emphasize how the history

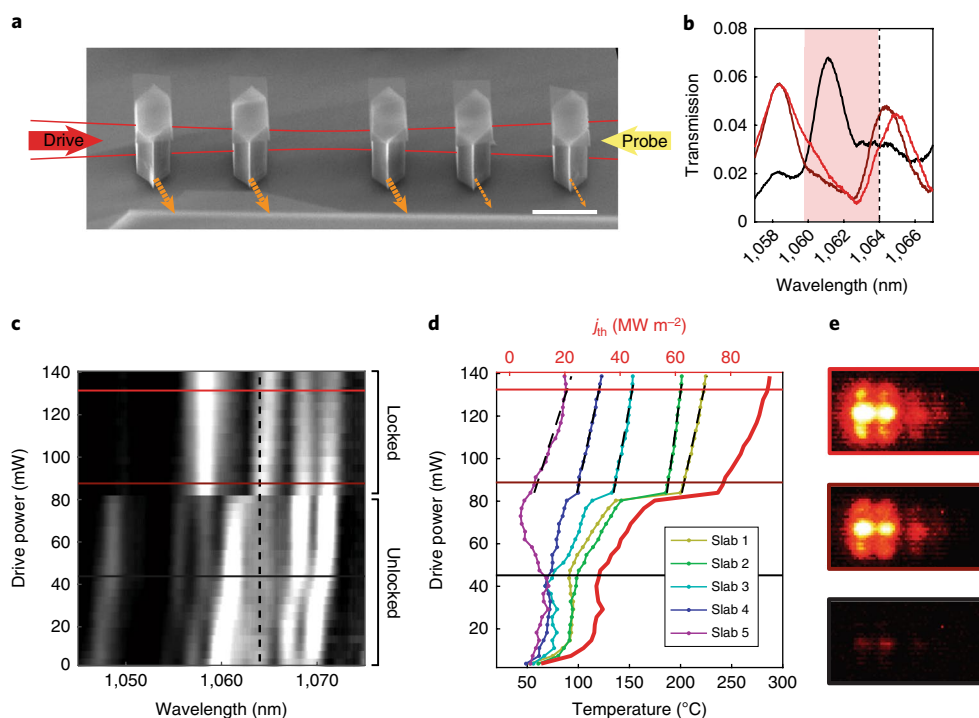


Fig. 2 | Phase transition to the organized steady state. **a**, Electron microscope image of five thermally insulated resonators (each dissipating heat, orange arrows), driven by a 1,064 nm laser (red arrow) and probed with a counter-propagating supercontinuum laser (yellow arrow). Scale bar, 20 μm . **b**, Transmission spectrum before (black curve) and after (dark red and red curves, at increasing drive powers) self-organization showing the emergence of a depletion band (shaded in red) fixed by the 1,064 nm drive (dashed line). **c**, Intensity plot of the transmission spectrum versus drive power (drive wavelength superimposed with dashed line) depicting the transition to the locked state. Horizontal lines correspond to the data slices in **b**. **d**, Temperature distribution of the five slabs versus drive power. The structure is heated above room temperature, using an out-of-plane blue laser, to improve contrast with the background. Cooperative heat dissipation is observed above the phase transition, where all temperatures linearly increase with drive power (fits shown as black lines). This transition corresponds with a sudden increase in the total dissipation (red curve). **e**, Thermal images of the structure at the three drive powers (outlined black to red, with colours corresponding to the powers in panels **b-d**).

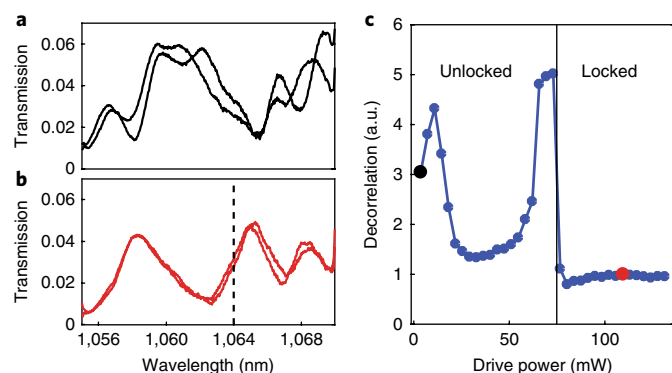


Fig. 3 | Resilience to thermal perturbation. **a**, Transmission spectra at two dynamic extrema when the undriven structure is exposed to thermal perturbation. **b**, Spectrum extrema under the same perturbation, but with the structure driven at 1,064 nm (dashed line) into the locked steady state. In this regime, the optical modes can each experience a different perturbation due to the non-uniform reorganization of thermal energy among the slabs (Supplementary Fig. 7a-c). **c**, Spectral decorrelation (normalized by the measured decorrelation of the locked state) as a function of pump power. Black and red data points correspond to data from **a** and **b**, respectively. The phase transition from the unlocked to the locked state is delineated with the black line.

of dissipation^{7,8} can trigger the emergence of new states and enable the storage of information through a collective memory.

In contrast with soft-matter systems, we have demonstrated that dissipative self-organization can occur without motion to produce self-adaptive behaviours in a solid-state photonic platform. We have shown the spontaneous phase ordering of a many-body structure, which efficiently dissipates the optical drive and displays a collective resiliency to thermal perturbations. By utilizing thermal imaging, we were able to directly observe the spontaneous organization of thermal dissipation and characterize its coordination. Our work might open routes for observing self-organization in inherently lossy material systems (for example, plasmonics³⁷). Collective organization can also be envisioned to address technological issues, such as for the self-correction to fabrication disorder³⁸ or the resiliency to environmental perturbations. Finally, dissipative self-organization in solid-state photonics may enable the physical realization of collective memory for perspectives in optics-based artificial intelligence and the emulation of collective behaviours of living matter¹⁰.

Online content

Any methods, additional references, Nature Research reporting summaries, source data, statements of data availability and associated accession codes are available at <https://doi.org/10.1038/s41566-018-0278-1>.

Received: 20 June 2018; Accepted: 12 September 2018;
Published online: 29 October 2018

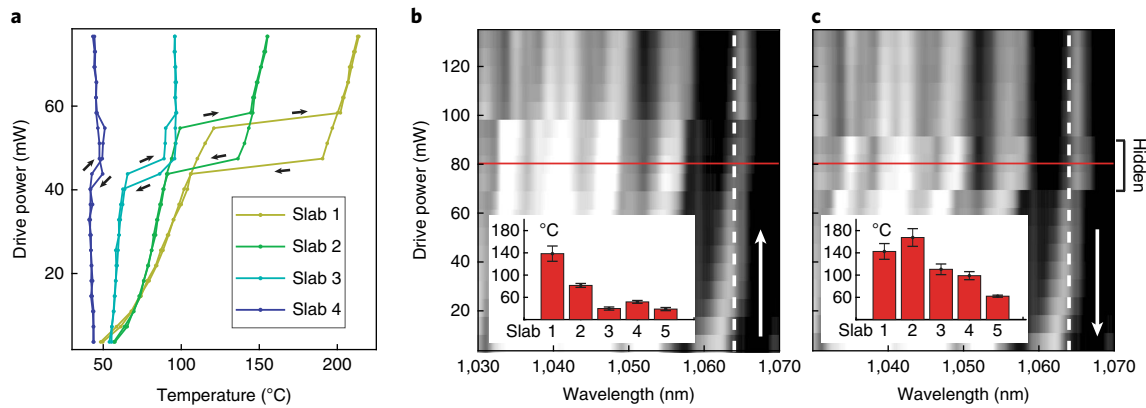


Fig. 4 | Collective memory effects and hidden states. **a**, Temperature profile showing hysteresis in a four-slab sample as a function of the adiabatically tuned drive power (arrows indicate increasing and decreasing power). The structure is slightly heated above room temperature using the blue laser to improve thermal contrast with the background. Spectral data are provided in Supplementary Fig. 8. **b,c**, The transmission spectrum of a five-slab sample with adiabatically increasing (**b**) and decreasing (**c**) pump power. A hidden state emerges when the drive power is decreased across the phase transition. Intensity plots are shown in log scale with the drive wavelength delineated in white. At 80 mW drive power (red line), the hidden state has a temperature profile (inset in **c**) different from the profile observed for increasing power (inset in **b**). Complete temperature data are included in Supplementary Fig. 8.

References

- Katz, Y., Tunström, K., Ioannou, C. C., Huepe, C. & Couzin, I. D. Inferring the structure and dynamics of interactions in schooling fish. *Proc. Natl Acad. Sci. USA* **108**, 18720–18725 (2011).
- Wu, X.-L. & Libchaber, A. Particle diffusion in a quasi-two-dimensional bacterial bath. *Phys. Rev. Lett.* **84**, 3017–3020 (2000).
- Dombrowski, C., Cisneros, L., Chatkaew, S., Goldstein, R. E. & Kessler, J. O. Self-concentration and large-scale coherence in bacterial dynamics. *Phys. Rev. Lett.* **93**, 098103 (2004).
- Narayan, V., Ramaswamy, S. & Menon, N. Long-lived giant number fluctuations in a swarming granular nematic. *Science* **317**, 105–108 (2007).
- Bricard, A., Caussin, J.-B., Desreumaux, N., Dauchot, O. & Bartolo, D. Emergence of macroscopic directed motion in populations of motile colloids. *Nature* **503**, 95–98 (2013).
- Sanchez, T., Chen, D. T. N., DeCamp, S. J., Heymann, M. & Dogic, Z. Spontaneous motion in hierarchically assembled active matter. *Nature* **491**, 431–434 (2012).
- England, J. L. Dissipative adaptation in driven self-assembly. *Nat. Nanotech.* **10**, 919–923 (2015).
- Perunov, N., Marsland, R. A. & England, J. L. Statistical physics of adaptation. *Phys. Rev. X* **6**, 021036 (2016).
- Yu, S., Wu, Y., Jeyasingh, R., Kuzum, D. & Wong, H. S. P. An electronic synapse device based on metal oxide resistive switching memory for neuromorphic computation. *IEEE Trans. Electron. Devices* **58**, 2729–2737 (2011).
- Wang, Z. et al. Memristors with diffusive dynamics as synaptic emulators for neuromorphic computing. *Nat. Mater.* **16**, 101–108 (2017).
- Fialkowski, M. et al. Principles and implementations of dissipative (dynamic) self-assembly. *J. Phys. Chem. B* **110**, 2482–2496 (2006).
- Mora, T. et al. Local equilibrium in bird flocks. *Nat. Phys.* **12**, 1153–1157 (2016).
- Whitesides, G. M. & Grzybowski, B. Self-assembly at all scales. *Science* **295**, 2418–2421 (2002).
- Beatus, T., Tlusty, T. & Bar-Ziv, R. Phonons in a one-dimensional microfluidic crystal. *Nat. Phys.* **2**, 743–748 (2006).
- Boekhoven, J. et al. Dissipative self-assembly of a molecular gelator by using a chemical fuel. *Angew. Chem. Int. Ed.* **122**, 4935–4938 (2010).
- Maiti, S., Fortunati, I., Ferrante, C., Scrimin, P. & Prins, L. J. Dissipative self-assembly of vesicular nanoreactors. *Nat. Chem.* **8**, 725–731 (2016).
- Kondepudi, D., Kay, B. & Dixon, J. End-directed evolution and the emergence of energy-seeking behavior in a complex system. *Phys. Rev. E* **91**, 050902 (2015).
- Snezhko, A. & Aranson, I. S. Magnetic manipulation of self-assembled colloidal asters. *Nat. Mater.* **10**, 698–703 (2011).
- Martinez-Pedrero, F., Ortiz-Ambriz, A., Pagonabarraga, I. & Tierno, P. Colloidal microworms propelling via a cooperative hydrodynamic conveyor belt. *Phys. Rev. Lett.* **115**, 138301 (2015).
- Souslov, A., Zuiden, B. C., van Bartolo, D. & Vitelli, V. Topological sound in active-liquid metamaterials. *Nat. Phys.* **13**, 1091–1094 (2017).
- Bachelard, N. et al. Emergence of an enslaved phononic bandgap in a non-equilibrium pseudo-crystal. *Nat. Mater.* **16**, 808–813 (2017).
- Rechtsman, M. C. et al. Photonic Floquet topological insulators. *Nature* **496**, 196–200 (2013).
- Choi, S. et al. Observation of discrete time-crystalline order in a disordered dipolar many-body system. *Nature* **543**, 221–225 (2017).
- Yariv, A. & Yeh, P. *Photonics: Optical Electronics in Modern Communications*. (Oxford Univ. Press, Oxford, 2006).
- Espinola, R. L., Tsai, M. C., Yardley, J. T. & Osgood, R. M. Fast and low-power thermo-optic switch on thin silicon-on-insulator. *IEEE Photon. Technol. Lett.* **15**, 1366–1368 (2003).
- Zhang, M., Shah, S., Cardenas, J. & Lipson, M. Synchronization and phase noise reduction in micromechanical oscillator arrays coupled through light. *Phys. Rev. Lett.* **115**, 163902 (2015).
- Heinrich, G., Ludwig, M., Qian, J., Kubala, B. & Marquardt, F. Collective dynamics in optomechanical arrays. *Phys. Rev. Lett.* **107**, 043603 (2011).
- Leonetti, M., Conti, C. & Lopez, C. The mode-locking transition of random lasers. *Nat. Photon.* **5**, 615–617 (2011).
- Tretiakov, K. V., Bishop, K. J. M. & Grzybowski, B. A. The dependence between forces and dissipation rates mediating dynamic self-assembly. *Soft Matter* **5**, 1279–1284 (2009).
- Snezhko, A., Aranson, I. S. & Kwok, W.-K. Structure formation in electromagnetically driven granular media. *Phys. Rev. Lett.* **94**, 108002 (2005).
- Osterman, N. et al. Field-induced self-assembly of suspended colloidal membranes. *Phys. Rev. Lett.* **103**, 228301 (2009).
- Uspal, W. E. & Doyle, P. S. Self-organizing microfluidic crystals. *Soft Matter* **10**, 5177–5191 (2014).
- Morin, A., Desreumaux, N., Caussin, J.-B. & Bartolo, D. Distortion and destruction of colloidal flocks in disordered environments. *Nat. Phys.* **13**, 63–67 (2017).
- Snezhko, A., Aranson, I. S. & Kwok, W.-K. Surface wave assisted self-assembly of multidomain magnetic structures. *Phys. Rev. Lett.* **96**, 078701 (2006).
- Timonen, J. V. I., Latikka, M., Leibler, L., Ras, R. H. A. & Ikkala, O. Switchable static and dynamic self-assembly of magnetic droplets on superhydrophobic surfaces. *Science* **341**, 253–257 (2013).
- Morin, A. & Bartolo, D. Flowing active liquids in a pipe: hysteretic response of polar flocks to external fields. *Phys. Rev. X* **8**, 021037 (2018).
- Maier, S. A. & Atwater, H. A. Plasmonics: localization and guiding of electromagnetic energy in metal/dielectric structures. *J. Appl. Phys.* **98**, 011101 (2005).
- Mookherjee, S., Park, J. S., Yang, S.-H. & Bandaru, P. R. Localization in silicon nanophotonic slow-light waveguides. *Nat. Photon.* **2**, 90–93 (2008).

Acknowledgements

This work was supported by the Laboratory Directed Research and Development Program (Non-Equilibrium Metamaterials, 18-174) of Lawrence Berkeley National Laboratory under US Department of Energy contract no. DE-AC02-05CH11231 for theory and optical design and measurement. Sample fabrication at the Molecular Foundry was supported by the Office of Science, Office of Basic Energy Sciences, of the US Department of Energy under contract no. DE-AC02-05CH11231. Support was

also provided by the King Abdullah University of Science and Technology Office of Sponsored Research (OSR) (award OSR-2016-CRG5-2950-03) for data analysis.

Author contributions

C.R. and N.B. designed and conducted experiments and performed the theoretical investigation. C.R. and D.B. performed sample fabrication. X.Z. and Y.W. guided the research. All authors contributed to writing the manuscript.

Competing interests

The authors declare no competing interests.

Additional information

Supplementary information is available for this paper at <https://doi.org/10.1038/s41566-018-0278-1>.

Reprints and permissions information is available at www.nature.com/reprints.

Correspondence and requests for materials should be addressed to X.Z.

Publisher's note: Springer Nature remains neutral with regard to jurisdictional claims in published maps and institutional affiliations.

© The Author(s), under exclusive licence to Springer Nature Limited 2018

Methods

Numerical model. We modelled the N dielectric resonators with randomly spaced slabs of identical thickness, $l = 10.5 \mu\text{m}$ (mean spacing = $30 \mu\text{m}$, s.d. of spacing = $4 \mu\text{m}$). The optical field that propagates through the system was computed with a transfer matrix (TM) method, in which each slab is associated with a complex refractive index, $n_i = n_i^{\text{re}} + in_i^{\text{im}}$, that is a function of the local temperature T_i (defined as the difference from room temperature). The evolution of local temperatures is described by the heat equations

$$\rho l C \frac{dT_i}{dt}(t) + 4h T_i(t) = P_i(t)$$

in which $P_i(t)$ (in W) is the absorbed power computed through TM simulation, $h = 40,000 \text{ W m}^{-2} \text{ K}^{-1}$ is the coefficient of thermal dissipation to the surroundings, estimated through 2D finite element modelling (FEM) simulation and weighted by a factor 4 to match the experimental time constant (Supplementary Fig. 6), $\rho = 2,330 \text{ kg m}^{-3}$ is the density of silicon and $C = 700 \text{ J kg}^{-1} \text{ K}^{-1}$ is the specific heat of silicon³⁹.

The modification of refractive indices with temperature was modelled by a linear increase in the real part, $n_i^{\text{re}} = 3.55 + \beta T_i$, and an exponential increase in the

imaginary part, $n_i^{\text{im}} = 0.8 \left(1 + \left(\frac{T_i}{295} \right)^b \right) \times 10^{-4}$, where $\beta = 2.2 \times 10^{-4} \text{ K}^{-1}$ and $b = 4.25$

correspond to the thermo-optic parameters of intrinsic silicon⁴⁰. Starting from elements at room temperature, the evolution of the system was obtained through an iterative approach. The absorbed intensity was computed for each slab at time t . Next, the distribution of temperature at time $t + \Delta t$, where $\Delta t = 1 \mu\text{s}$ is the time step in our simulation, is given by

$$T_i(t + \Delta t) = T_i(t) \left(1 - \frac{4h}{\rho l C} \Delta t \right) + \frac{P_i(t)}{\rho l C} \Delta t$$

The calculated new temperatures were fed back into the TM model through a modification of the refractive indices.

The thermal confinement within the resonators was modelled through FEM simulations (Supplementary Fig. 2a). Silicon was modelled with a thermal conductivity of $\lambda_{\text{Si}} = 149 \text{ W m}^{-1} \text{ K}^{-1}$, and the layer of silicon oxide by a conductivity of $\lambda_{\text{SiO}_2} = 1.4 \text{ W m}^{-1} \text{ K}^{-1}$. In a two-element array, a source term was introduced on the first slab to mimic its optical absorption. The thermal loss coefficient h was estimated from the linear increase of the temperature of the first slab with optical absorption. From this simulation we calculated the expected crosstalk between elements induced by conduction through the substrate, which is estimated to be about 4%.

Sample fabrication. Samples were fabricated through anisotropic wet etching of silicon-on-insulator chips with a $15 \mu\text{m}$ [110]-oriented device layer and a $1.5 \mu\text{m}$ oxide layer (Supplementary Fig. 2b). This oxide layer promotes thermal insulation, which is required to reach high temperatures. A silicon nitride hard mask (100 nm thick) was grown on the wafers first using low-pressure chemical vapour deposition and then chips were patterned using ultraviolet photolithography (ma-P 1215 photoresist and ma-D 533/S photodeveloper) and reactive-ion etching (SF_6 and O_2). Structures were patterned at chip edges and oriented along the [110] crystal axes.

Slab thickness and spacing were varied from sample to sample. The width of all slabs started out at $120 \mu\text{m}$ and were sacrificially etched to around $30 \mu\text{m}$ during wet etching, achieved using a 30% KOH solution (80°C). After etching, all slabs were $15 \mu\text{m}$ tall, which was achieved using the oxide layer as an etch stop. KOH etching of [110]-oriented silicon wafers exposed the [111] crystalline faces⁴¹, which can be used to create high-quality Fabry-Pérot resonators⁴². After KOH etching, the slabs were partially undercut using buffered 10:1 HF to improve the thermal insulation from the substrate. The sample geometry used to collect data for Figs. 2 and 3, Fig. 4a, and Fig. 4b, respectively, consisted of slabs defined to be 12, 16, and $16 \mu\text{m}$ thick with [22.7, 20.5, 10.5, 22.7], [28, 30, 26] and [19.5, 19.5, 19.5, 19.5] μm centre-to-centre spacings. In general, slabs with thickness below $10 \mu\text{m}$ are difficult to use as the accumulated phase across the slabs scales with thickness, and the higher power required to observe a phase transition readily burns the sample. Thermal radiation between elements separated by tens of micrometres is greatly limited⁴³, which in the ideal case of blackbody emitters (assuming 200°C temperature difference) contributes to heat flow orders of magnitude smaller than the heat conduction through the substrate.

Optical set-up. Samples were mounted to a gimbal stage and oriented co-axially with the continuous-wave drive laser ($1,064 \text{ nm}$, horizontally polarized). The drive laser had a Gaussian profile focused to a $5 \mu\text{m}$ beam diameter with a $170 \mu\text{m}$ Rayleigh range. This beam profile under-filled the slabs, which were $15 \mu\text{m}$ tall and $30 \mu\text{m}$ wide (inset, Supplementary Fig. 2b), and whose array extended no deeper than $150 \mu\text{m}$ from the edge of the chip. A counter-propagating probe beam consisting of a home-built supercontinuum laser ($1,000\text{--}1,090 \text{ nm}$, vertically polarized) was used to illuminate the sample from behind. The probe laser heated the sample negligibly, as its power was maintained below 10 mW with a fluence spread over eight times the area of the drive. The probe laser was passed into a confocal set-up using a polarizing beamsplitter and sent to an infrared spectrometer for transmission measurements. We fully removed the drive laser from the spectrum by time gating the spectrometer. The drive laser was turned off for $20 \mu\text{s}$ every 1 ms , during which time the spectrometer was triggered to measure the spectrum. This $20 \mu\text{s}$ window is much shorter than the $120 \mu\text{s}$ thermalization time of the structure (Supplementary Fig. 6c,d), ensuring that our measurements corresponded well with the steady-state response of our system.

A third laser (100 mW , 450 nm) was focused onto the sample to both raise the temperature of the slabs above room temperature (for better thermal visualization against background) and to temporally perturb the structure. For the perturbation studies performed in Fig. 3 this laser was modulated at 1 Hz using a rotating neutral density filter wheel. We acquired 1,000 transmission spectra (S_i) spanning approximately 17 cycles of the blue laser. The decorrelation was then calculated by $1 - \langle \rho_{ij}(S_i, S_j) \rangle$, in which $\langle \rho_{ij}(S_i, S_j) \rangle$ stands for the mean value of the correlation between all the measured spectra. Thermal images of the structure were acquired using an infrared camera (Goodrich SU640HSX) with a $1,400 \text{ nm}$ long-pass filter.

Thermal measurement. The steady-state temperatures of each slab were measured from the intensity profile of their thermal images. Since the random position of each slab along the array is known, we fitted the image to multiple Lorentzian curves and calculated the thermal radiation intensity (Supplementary Fig. 5c). This fitted intensity was mapped to an absolute temperature using a calibration curve, obtained from measuring the response of isolated slabs (Supplementary Fig. 5b). We measured both the thermal image profile and the transmission spectrum of three separate isolated slabs as a function of increasing drive power (Supplementary Fig. 5a). The absolute temperature was calculated relative to room temperature using the spectral shift of a single slab, which was fitted to a Fabry-Pérot response. This calculation assumes a thermo-optic coefficient for silicon of $\beta = 2.2 \times 10^{-4}$, which is expected to be constant over our temperature range⁴⁴, and a room-temperature refractive index of 3.55. The different responses of the three different isolated slabs were used to quantify error bars for our calibration curve. Experimental errors (insets in Fig. 4b,c and Supplementary Figs. 8 and 5c) were calculated by combining the calculated uncertainties (in standard error) from the Lorentzian fit and the absolute temperature calibration—the latter of which is the dominant source of error due to slab-to-slab variability in both thickness and thermal radiation intensity.

Data availability

The data that support the plots within this paper and other findings of this study are available from the corresponding author upon reasonable request.

References

- Carmon, T., Yang, L. & Vahala, K. J. Dynamical thermal behavior and thermal self-stability of microcavities. *Opt. Express* **12**, 4742–4750 (2004).
- Green, M. A. Self-consistent optical parameters of intrinsic silicon at 300 K including temperature coefficients. *Sol. Energy Mater. Sol. Cells* **92**, 1305–1310 (2008).
- Hölke, A. & Henderson, H. T. Ultra-deep anisotropic etching of (110) silicon. *J. Micromech. Microeng.* **9**, 51 (1999).
- Lipson, A. & Yeatman, E. M. Low-loss one-dimensional photonic bandgap filter in (110) silicon. *Opt. Lett.* **31**, 395–397 (2006).
- Fu, C. J. & Zhang, Z. M. Nanoscale radiation heat transfer for silicon at different doping levels. *Int. J. Heat Mass Transf.* **49**, 1703–1718 (2006).
- Yamada, S., Song, B.-S., Asano, T. & Noda, S. Experimental investigation of thermo-optic effects in SiC and Si photonic crystal nanocavities. *Opt. Lett.* **36**, 3981–3983 (2011).